Breakup threshold anomaly in the elastic scattering of the ^{9}Be + ^{80}Se system

F. Gollan [a,b,*], D. Abriola [a], A. Arazi [a,b], O.A. Capurro [a], M.A. Cardona [a,b], E. de Barbará [a], D. Hojman [a,b], G.V. Martí [a], A.J. Pacheco [a,b], D. Rodrigues [a,b], J.E. Testoni [a]

[a] *Laboratorio TANDAR, Comisión Nacional de Energía Atómica, Av. Gral. Paz 1499, BKNA1650 San Martín, Argentina*
[b] *Consejo Nacional de Investigaciones Científicas y Técnicas, Av. Rivadavia 1917, C1033AAJ Buenos Aires, Argentina*

Abstract

Elastic scattering angular distributions for the ^{9}Be + ^{80}Se system were measured at eleven energies from below to above the Coulomb barrier. The experimental elastic scattering cross sections were analyzed within the framework of the optical model to study the energy dependence of the potential. Two different potentials were used: an energy-dependent phenomenological Woods–Saxon potential and a double folding São Paulo potential. For these two potentials, the energy dependence of the real and imaginary strengths shows consistent with the presence of the breakup threshold anomaly. An alternative method is proposed for calculating the dispersion relation between the real and imaginary parts of the optical potential based on bivariate random sampling obtained from the covariance matrix of the adjusted experimental angular distributions.
© 2018 Elsevier B.V. All rights reserved.

---

* Corresponding author.
E-mail addresses: gollan@tandar.cnea.gov.ar (F. Gollan), abriola@tandar.cnea.gov.ar (D. Abriola).

1. Introduction

In the past years, a great experimental and theoretical effort has been done to understand the mechanisms involved in the reactions induced by weakly bound nuclei at energies around the Coulomb barrier. In particular, the effects of the breakup channel on the elastic scattering and fusion have been studied extensively for both stable (^{9}Be, ^{6}Li, ^{7}Li) and unstable (^{6}He, ^{7}Be, ^{8}Li, ^{8}B, etc.) weakly bound projectiles [1]. It is well known that the optical potential parameters that describe the elastic scattering for the case of tightly bound nuclei projectiles shows a rapid variation as a function of the energy near the Coulomb barrier, a phenomenon referred to as threshold anomaly (TA) [2,3]. This manifests as a rapid decrease in the strength of the imaginary potential at energies below the Coulomb barrier, while the real potential increases and shows a bell-shaped maximum in this region. This anomaly is attributed to the coupling of nonelastic channels to the elastic channel that produces an attractive dynamic polarization potential. The decrease of the imaginary potential is associated with the closing of nonelastic peripheral channels at sub-barrier energies due to Coulomb repulsion. The correlation between the real and the imaginary potentials is due to causality that imposes the condition that no scattered wave emerges before the incident wave reaches the target. The mathematical relation involving causality and the TA is the dispersion relation, which connects the real and imaginary potentials through a principal value integral [2,3]. As opposed to tightly bound nuclei, for which the TA has been conclusively demonstrated, studies involving weakly bound nuclei have produced some contradictory results [4–20]. It has been suggested [13,21] that the effect of coupling to the breakup channel may produce a repulsive polarization potential which affects the overall dynamic potential and could inhibit the manifestation of the usual TA. For systems in which one of the participants is a weakly bound nucleus, a new kind of anomaly has been proposed [7,14,22,23], justified via dispersion relations in [14] and named later as breakup threshold anomaly (BTA) [8,24]. The coupling of the breakup channel, even at energies below the Coulomb barrier, would be reflected as an increase of the imaginary potential as a function of the decreasing energies. As a consequence of the dispersion relation, this implies a decrease in the real part of the optical potential.

A behavior compatible with the BTA has in fact been observed in the reactions induced by ^{6}Li on ^{58}Ni [9], ^{80}Se [10], ^{144}Sm [11] and ^{208}Pb [8], and also for ^{9}Be + ^{64}Zn [15]. On the other hand, reactions with ^{7}Li projectiles on ^{59}Co [12], ^{80}Se [10], ^{138}Ba [7], ^{144}Sm [11] and ^{208}Pb [13] show the presence of the usual TA. Finally, in several other reactions involving these stable weakly bound projectiles, no definite conclusions could be drawn regarding any of these two types of behavior. This includes the cases of ^{6}Li on ^{27}Al [4], ^{64}Ni [5], ^{112}Sn, ^{116}Sn [6], ^{138}Ba [7], ^{7}Li + ^{28}Si [14], and ^{9}Be on ^{12}C [20], ^{27}Al [16], ^{120}Sn [25] and ^{144}Sm [17].

Among the main experimental limitations for establishing the character of the anomaly is the difficulty to obtain enough experimental data near and below the barrier. In this region, the elastic scattering is dominated by the Coulomb interaction, so high-precision cross-section measurements are required in order to assess any deviation from the Rutherford angular distribution.

To establish robust conclusions regarding the threshold anomaly of the optical potential around the Coulomb barrier it is necessary to analyze the experimental data in the frame of different potential models. Among the most commonly used models are the phenomenological Woods–Saxon potential [11,26] and the microscopic, non-local, double-folding São Paulo [27]. The physical interpretation should be independent of this choice. Not less important, an unambiguous determination of the kind of anomaly requires a rigorous criterion for the assessment of the parameter uncertainties in terms of experimental ones [28].

The purpose of the present work is to contribute to the understanding of the energy behavior for systems involving weakly bound projectiles at near-barrier energies. With this aim, we have measured elastic-scattering angular distributions for the ^{9}Be + ^{80}Se system at eleven energies around the Coulomb barrier. The target was chosen for its intermediate mass, between those of ^{27}Al and ^{120}Sn, targets which were already studied with this projectile [16,25]. The results were analyzed with a phenomenological Woods–Saxon potential and a double-folding São Paulo potential. We also present a new method based on random sampling to determine if the real and imaginary potentials obtained follow a behavior compatible with the dispersion relation.

This article is organized as follows. In Sec. 2 the experimental setup is described as well as the obtained elastic-scattering angular distributions. In Sec. 3 the data are analyzed in the framework of the two potentials and their outcomes are compared. Summary and conclusion are given in section 4.

2. Experimental details

Experimental elastic scattering angular distributions were measured at eleven bombarding energies: 17, 18, 19, 20, 21, 22, 23, 24, 25, 30, and 32.8 MeV in the laboratory frame. The nominal value of the Coulomb barrier is estimated in 20 MeV (18 MeV in c.m.) by empirical models [29]. Beams of ^{9}Be were delivered by the 20UD tandem accelerator of the TANDAR Laboratory in Buenos Aires. The beam was defined by two rectangular collimators (3.5 mm × 4.5 mm) upstream the scattering chamber. Enriched (99.8%) ^{80}Se targets, 110 µg/cm^2 thick, evaporated onto 20 µg/cm^2 thick carbon foils, were placed at the center of a 70-cm-diameter scattering chamber. The target was set at $+40°$ $(-40°)$ with respect to the beam direction for the measurement at forward (backward) angles. In the data analysis, the beam energies were corrected for the energy lost (about 60 keV), assuming the scattering takes place in the middle of the target.

The detection system consisted of an array of eight surface-barrier silicon detectors with an angular separation of 5° between adjacent detectors. The detectors were mounted on a rotating support on the bottom of the scattering chamber. The angular distributions were taken in angular steps between 1° and 5°, depending on the energy and angular range. A second set of two surface-barrier detectors with an angular separation of 8° was placed on a rotating support at the top of the chamber to detect reaction products at backward angles. Rectangular slits defined the angular acceptance of each detector, with solid angles ranging from 0.1 msr (most forward detector) to 0.6 msr (most backward one). This allowed comparable counting rates in all detectors. The energy resolution (FWHM) ranged from 0.5 to 0.8%, which was appropriate to identify and separate the inelastic-excitation peak corresponding to the first excited state of the ^{80}Se nucleus (2^+, 0.667 MeV) from the elastic peak (see Fig. 1). As can be seen, there is no significant background affecting the elastic peak. The same negligible background is seen at other energies. This was also the case in previous work with ^{9}Be [25], where it was shown that α particles arising from breakup have lower energies than the elastic peak.

Two monitor detectors were fixed at different hemispheres at 16° with respect to the beam direction. The angular acceptance of both detectors was 0.25° defined by circular collimators. To avoid any possible shadowing of a monitor due to the edge of the target ladder, measurements performed at forward (backward) scattering angles were normalized using the monitor at the same (opposite) hemisphere as the detector array. Assuming that the scattering at the monitor angles is purely Rutherford for all studied energies, the elastic scattering differential cross sections is obtained as
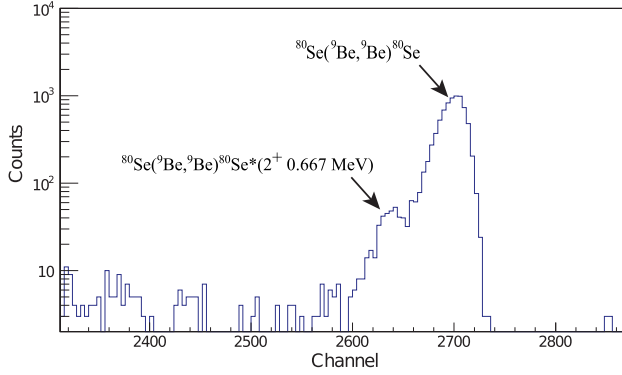
Fig. 1. Energy spectrum of the reaction products for the ^{9}Be + ^{80}Se system, obtained at $E_{\text{lab}} = 30$ MeV, $\theta_{\text{lab}} = 55°$. Elastic and inelastic peaks can be distinguished.

$$\frac{d\sigma}{d\Omega}(\theta_{\text{det}}) = \frac{d\sigma_{\text{Ruth}}}{d\Omega}(\theta_{\text{mon}}) \frac{N_{\text{det}}}{N_{\text{mon}}} \frac{J(\theta_{\text{det}})}{J(\theta_{\text{mon}})} \frac{\Omega_{\text{mon}}}{\Omega_{\text{det}}} \tag{1}$$

where $\frac{d\sigma_{\text{Ruth}}}{d\Omega}(\theta_{\text{mon}})$ is the differential Rutherford cross section at the monitor angle, N_{det} and N_{mon} are the number of events, $J(\theta_{\text{det}})$ and $J(\theta_{\text{mon}})$ are the Jacobians and $\Omega_{\text{mon}}/\Omega_{\text{det}}$ is the solid angle ratio between the monitor and the detector. These ratios were obtained from the scattering of ^{9}Be and ^{16}O on a ^{197}Au target (250 μg/cm^2) at energies well below the corresponding Coulomb barrier by means of Eq. (1).

A Faraday cup at the end of the beam line, far away from the target, was used to integrate the total charge delivered by the beam. This integrated current, together with geometrically determined solid angles, the known target thickness, and the average charge state of the ion after going through the target, allowed an alternative method to corroborate the assumption of purely Rutherford scattering on the monitors at the highest energies.

In Fig. 2 the angular distributions for all measured energies of the elastic scattering cross sections, normalized to the Rutherford cross sections are displayed. The uncertainties were calculated taking into account the statistical and systematic contributions. The statistical uncertainty considered the number of counts in the detector and in the monitor and was typically in the range of 0.2–2.0%, except for the higher energies and backward angles for which uncertainty values up to 10% were obtained. The uncertainties in the solid-angle ratios $\Omega_{\text{mon}}/\Omega_{\text{det}}$ where included in error bars.

3. Data analyses and results

3.1. Optical model analysis

The experimental angular distributions were described in the framework of the optical model using a phenomenological potential given by

$$U(r) = -Vf(r, r_0, a) - iW_i f^2(r, r_{i0}, a_i) - iW_{si} g(r, r_{si0}, a_{si}) \tag{2}$$

where f is the Woods–Saxon factor for the real part
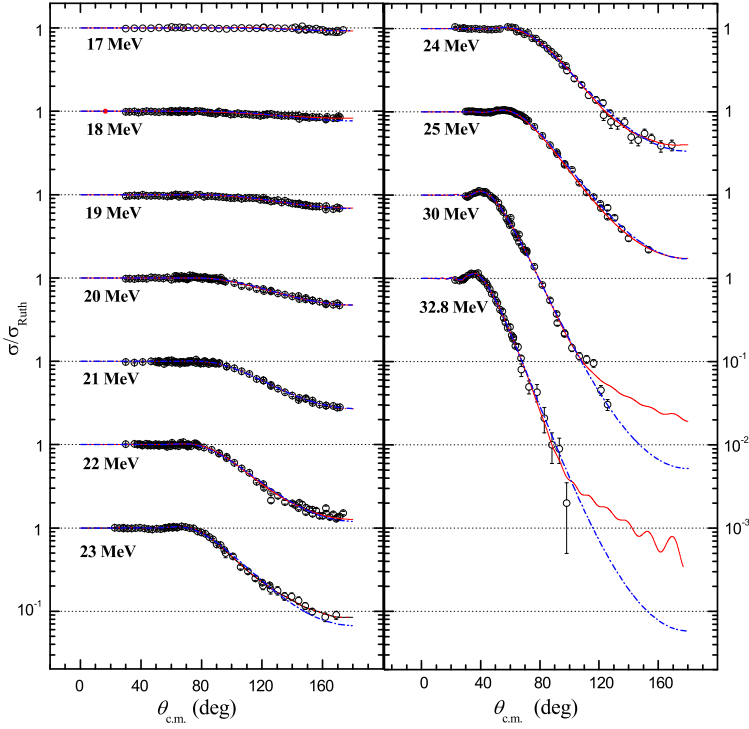
$$f(r, r_0, a) = \frac{1}{1 + e^{\frac{r-R}{a}}} \tag{3}$$

Fig. 2. Elastic scattering cross sections normalized to the Rutherford cross sections for the ^{9}Be + ^{80}Se system and optical model calculations. The full lines (red) correspond to Woods–Saxon energy-dependent with variable geometry. The dash–dot (blue) corresponds to a São Paulo potential (for energies below 22 MeV, both fits are almost indistinguishable). (For interpretation of the colors in the figure(s), the reader is referred to the web version of this article.)

$R = r_0(A_p^{1/3} + A_t^{1/3})$, where r_0 and a are the real reduced radius and diffuseness (geometric parameters), and A_p and A_t are the projectile and target mass number. The same expressions are obtained for the reduced radii of the imaginary potential. The first term of Eq. (2) represents the real nuclear potential $V(r)$. The second term represents the volume contribution to the imaginary potential and is proportional to the square of the Woods–Saxon factor. It simulates the incoming wave boundary condition and accounts for fusion [30]. The third term corresponds to the surface part of the imaginary potential which is proportional to the derivative of the Woods–Saxon shape

$$g(r, r_{si0}, a_{si}) = -4a_{si}\, df(r, r_{si0}, a_{si})/dr \qquad (4)$$

and takes into account the absorption due to peripheral reactions.

The phenomenological potential parameters were calculated under three different conditions: a) energy-independent (EI) potential, b) energy-dependent potential with fixed geometric parameters (EDFG), and c) an energy-dependent potential with variable geometric parameters (EDVG). The volume parameters of the imaginary potential W_i, r_{i0} and a_i were kept fixed in all cases with values of $W_i = 10$ MeV, $r_{i0} = 1.0$ fm and $a_i = 0.15$ fm. These geometrical values are lower than the real and surface imaginary components, as shown below for the geometrical parameters obtained for the EI, EDFG and EDVG cases. Thus, the volume imaginary potential term does not contribute significantly in the outer nuclear region. For every potential condition, the adjusted

Table 1

Parameters of the energy independent potential (EI). The projectile energy, V, W_i and W_{si} are in MeV, the reduced radii and diffuseness are in fm and the volume integrals per nucleon pair are in MeV fm^3. The global estimator of the fit $\sum_{k=1}^{n} \chi_k^2 N_k / (\sum_{i=k}^{n} N_k - p)$ is 2.817, where $p = 6$ is the number of parameters fit and the index k stands for each particular energy.

$E_{c.m.}$	V	r_0	a	W_i	r_{i0}	a_i	W_{si}	r_{si0}	a_{si}	$[G(E)]_V$	$[G(E)]_W$	χ^2/ν
15.2												0.524
16.1												4.448
17.0												1.979
17.9												1.950
18.8												2.901
19.7	33.91	1.264	0.563	10.0	1.0	0.15	2.40	1.451	0.542	4.27	3.04	4.037
20.6												2.035
21.5												1.309
22.4												2.312
26.9												4.098
29.4												4.500

Table 2

Parameters of the energy dependent potential with fixed geometry (EDFG). The projectile energy, V, W_i and W_{si} are in MeV, the reduced radii and diffuseness are in fm and the volume integrals per nucleon pair are in MeV fm^3. The global estimator of the fit $\sum_{i=1}^{n} \chi_i^2 / (\sum_{i=1}^{n} N_i - p)$ is 1.984, where $p = 2$ is the number of parameters fit.

$E_{c.m.}$	V	r_0	a	W_i	r_{i0}	a_i	W_{si}	r_{si0}	a_{si}	$[G(E)]_V$	$[G(E)]_W$	χ^2/ν
15.2	189.37						0.11			23.76	0.13	0.362
16.1	−99.94						8.23			−12.54	10.40	2.496
17.0	−17.10						4.74			−2.15	5.99	1.941
17.9	14.82						3.64			1.86	4.64	1.455
18.8	32.27						2.26			4.05	2.86	2.494
19.7	42.76	1.264	0.563	10.0	1.0	0.15	2.48	1.451	0.542	5.36	3.13	2.966
20.6	37.51						1.91			4.71	2.41	1.791
21.5	33.08						2.60			4.15	3.29	1.305
22.4	35.42						2.19			4.44	2.77	2.846
26.9	33.89						1.85			4.25	2.34	2.323
29.4	35.77						1.28			4.49	1.61	1.193

parameters were obtained from a m-grid search, where m stands for the number of parameters fit. The calculations based on the phenomenological potential were performed with the code PTOLEMY [31].

The energy-independent (EI) Woods–Saxon potential was used to perform a first and simultaneous fit to the data at all energies by adjusting the real and surface imaginary parameters (V, r_0, a, W_{si}, r_{si0} and a_{si}). The obtained parameters and the resulting χ^2/ν of the fits are presented in Table 1. Here, $\nu = N - p$ is the number of degrees of freedom, being N the number of data points per energy, and p the number of parameters fit ($p = 6$ in this case). The following step is to consider an energy-dependent potential with fixed geometry (EDFG). This was accomplished by fitting the real and surface imaginary depths (V and W_{si}) as a function of the energy, keeping fixed all geometrical parameters at the values obtained in the EI case. The values of the real and surface-imaginary depths are presented in Table 2, as well as the constant reduced radii and diffuseness (that were kept constant). As can be seen in the χ^2/ν values, the EDFG condition shows a significant improvement to the adjustment of the parameter data respect to the EI case. The last

Table 3
Parameters potential of the energy dependent with variable geometry (EDVG). The projectile energy, V, W_i and W_{si} are in MeV, the reduced radii and diffuseness are in fm and the volume integrals per nucleon pair are in MeV fm^3. The global estimator of the fit $\sum_{i=1}^{n} \chi_i^2 / (\sum_{i=1}^{n} N_i - p)$ is 1.532, where $p = 6$ is the number of parameters fit.

$E_{\text{c.m.}}$	V	r_0	a	W_i	r_{i0}	a_i	W_{si}	r_{si0}	a_{si}	$[G(E)]_V$	$[G(E)]_W$	χ^2/ν
15.2	29.71	1.299	0.786				1×10^{-03}	1.514	0.423	8.15	2×10^{-03}	0.418
16.1	−8.55	1.350	0.970				4.92	1.382	0.705	−3.55	5.37	1.837
17.0	9.24	1.280	0.418				3.51	1.350	0.701	0.77	3.49	1.866
17.9	13.84	1.293	0.482				2.77	1.499	0.511	1.78	3.70	1.519
18.8	16.01	1.212	0.696				1.55	1.452	0.629	1.92	2.07	2.419
19.7	12.40	1.248	0.792	10.0	1.0	0.15	2.41	1.429	0.578	2.45	2.93	2.463
20.6	20.23	1.300	0.552				1.79	1.544	0.398	3.16	2.12	1.058
21.5	19.53	1.237	0.578				2.36	1.521	0.471	2.00	3.70	1.175
22.4	35.09	1.264	0.538				1.70	1.529	0.407	4.05	2.08	1.457
26.9	36.31	1.238	0.601				1.87	1.455	0.511	4.04	2.34	2.178
29.4	40.05	1.220	0.608				1.34	1.449	0.547	3.86	1.69	1.014

phenomenological case was constructed taking the EDFG results as a reference and allowing the geometrical values to slightly change around those values. In this way, an energy-dependent variable geometry (EDVG) potential was obtained. As can be seen in Table 3, a better adjustment has been obtained with this configuration for all energies with overall small parameter variations, except for the lower energies, where there is an increase of the real diffuseness. The uncertainties, corresponding to a confidence level of 68%, in the parameters for the EI, EDFG and EDVG potentials were obtained by varying the parameters until the total χ^2 is increased by $\Delta\chi^2 \chi_0^2/\nu$. Here χ_0^2 is the minimum value of χ^2 and the factor $\Delta\chi^2$ is equal to 2.3 and 7.04 for two and six parameters, respectively [28,32].

The following step consisted in the evaluation of the energy dependence of the real and imaginary parts of the optical potential. Since the potential shape changes with different energies, it is useful to study their behavior at the sensitivity radius R_S [30]; this corresponds to the radius where the elastic scattering is most sensitive to the values of the potential depths V and W. At each energy, the value of R_S was determined by selecting a set of slightly modified diffuseness parameters a (taken in steps of 0.05 fm around the best value) and adjusting the reduced radius and potential depth to fit the data with χ^2/ν similar to the optimal value. Finally, the sensitive radius was obtained from the intersection of these potentials. The same procedure was performed to obtain the imaginary sensitive radius, varying the surface diffuseness a_{si}. Even though one can expect a single crossing point for all potentials, that is not always the case. Therefore, the value of R_S for each energy was obtained by minimizing the estimator of the variance of the sample, defined by

$$s^2(r) = \frac{1}{n-1} \sum_{i=1}^{n} (V_i(r) - V_{min}(r))^2 \tag{5}$$

as a function of the radius. The index i stands for each particular potential, which corresponds to a given value of diffuseness. The same procedure was done for the imaginary potential. Fig. 3 shows the crossing points of the real and imaginary potentials for the different adjustments with similar χ^2/ν, corresponding to the fit of the $E_{\text{c.m.}} = 26.9$ MeV with the EDVG potential.

It was observed that for all energies, the real sensitivity radius fluctuated considerably in the region 8.6 fm $\leq r \leq$ 9.1 fm and the imaginary in 9.6 fm $\leq r \leq$ 10.5 fm. Therefore, a unique value
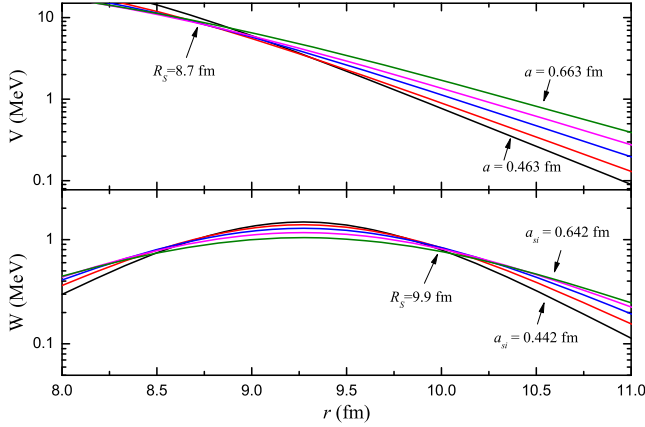
Fig. 3. Sensitivity radius of the real and imaginary parts of the Woods–Saxon EDVG at $E_{c.m.} = 26.9$ MeV estimated by the crossing point of different fits with similar χ^2/ν value. The real and imaginary diffuseness, a and a_{si} were varied in steps of 0.05 fm.

could not be established. To overcome the problem, the method proposed by Brandan et al. [33] was applied where the potential is replaced by the volume integral per nucleon pair weighted by a Gaussian function $\phi(r)$, centered on an average value of $\overline{R}_S$ with a width σ. The two volume integrals are $[G(E)]_V$ and $[G(E)]_W$, where W is the sum of the volume and the surface components of the imaginary potential. The volume integral for the real potential is given by the expression

$$[G(E)]_V = \frac{1}{A_p \times A_t} \int V(r, E)\phi(r)4\pi r^2 dr \qquad (6)$$

where A_p and A_t are the projectile and target mass numbers respectively. An important property is that the dispersion relation still holds for the volume integrals, as it was shown by Mahaux et al. [34,35] and has an expression in the form of

$$[G(E)]_V = \frac{P}{\pi} \int \frac{[G(E')]_W}{E' - E} dE' \qquad (7)$$

where P denotes principal value. To calculate the parameters of the Gaussian distribution $\phi(r)$, a normal distribution has been assumed for the sensitivity radius. The average radius was calculated without taking into account the lower energies 15.2 and 16.1 MeV, where they deviate considerably from the average value. The obtained value for the EDVG potential is $\overline{R}_S = 9.59$. The standard deviation value was set to 0.5 fm. This choice was made to include the most significant contributions from the region where the potentials have been evaluated. The results of these integrals are shown in Fig. 4.

The volume integral for the real part of the energy-dependent potential shows a decrease for energies below the Coulomb barrier. In the same region, the imaginary part increases in strength. For the lowest studied energy ($E_{c.m.} = 15.2$ MeV) this behavior is inverted and the imaginary integral vanishes, reflecting the definitive closure of all inelastic reaction channels. On the other hand, the elastic scattering cross section corresponds to almost pure Rutherford at this energy and, consequently, increases the difficulty of determining the values of the potentials at a given uncertainty level.
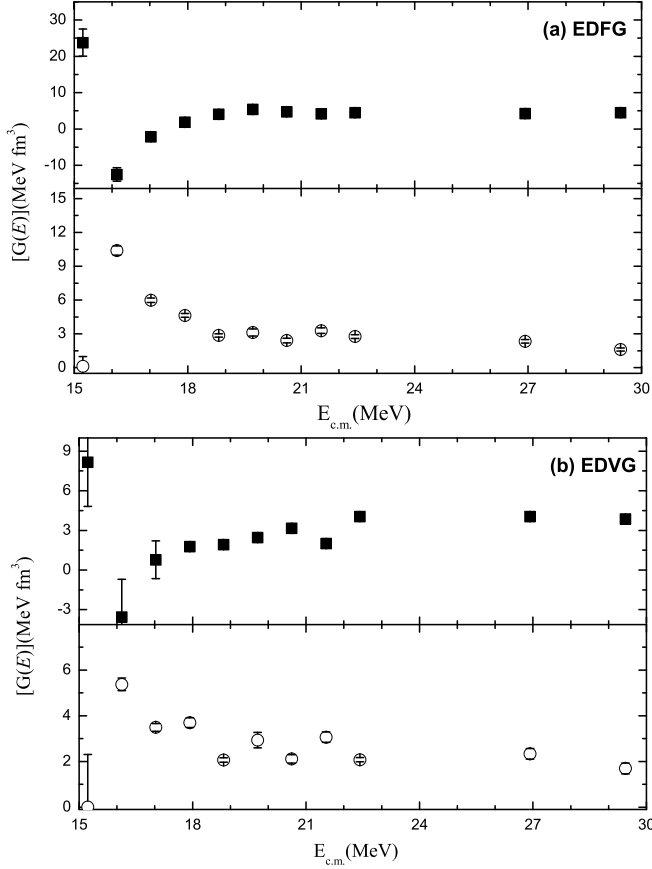
Fig. 4. Volume integrals per nucleon $[G(E)]$ Eq. (7) around the sensitivity radius calculated for the real (squares) and imaginary (circles) parts of the Woods–Saxon potentials. The figures (a) and (b) corresponds to the EDFG and EDVG potentials respectively. Uncertainty bars do not include the systematic components from R_S and σ. Calculations with slightly different values for R_S (up to 5%) and up to a factor of two for σ were performed with no significant difference in the energy behavior of the integrals.

The elastic scattering cross sections were also analyzed using the São Paulo potential. This global parameter-free optical potential [36–38] was chosen because it has been successfully used to describe a large variety of systems in a wide energy range. The normalized expression for the São Paulo potential used in the present analysis can be obtained from the following expression [8,24]

$$V_{SP}(R, E) = [N_R(E) + i N_I(E)]V_{LE}(R, E), \tag{8}$$

where $V_{LE}(R, E)$ is the local equivalent potential. The explicit energy dependence of $V_{LE}(R, E)$ results from the local equivalence of the otherwise nonlocal interaction [39], it is not dispersive and incorporates the double folding potential. The coefficients $N_R(E)$ and $N_I(E)$ are energy-dependent factors that take into account the effects of the dynamic polarization potentials (DPP) arising from direct channel couplings. An important property is that the DPPs are dispersive, with the real and imaginary parts being connected through a dispersion relation [8].

Table 4

Normalization factors for the real and imaginary parts of the São Paulo potential. The projectile energy is in MeV and the volume integrals per nucleon pair are in MeV fm^3. The integrals were evaluated at the sensitivity radius R_S. The global estimator of the fit $\sum_{i=1}^{n} \chi_i^2 / (\sum_{i=1}^{n} N_i - p)$ is 1.939, where $p = 2$ is the number of parameters being fit.

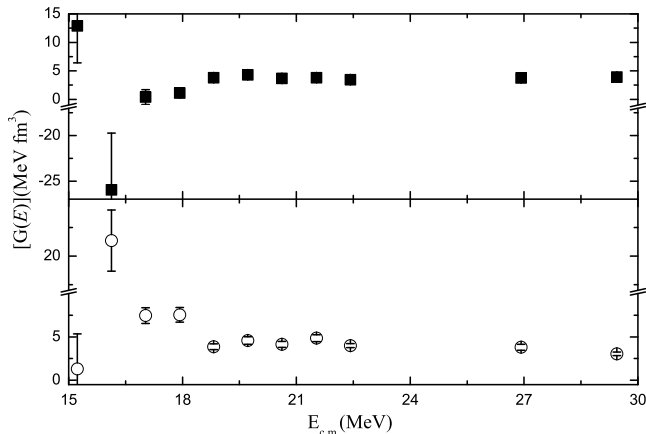| $E_{c.m.}$	N_R	N_I	$[G(E)]_V$	$[G(E)]_W$	χ^2/ν
15.2	3.70	0.38	12.91	1.31	0.369
16.1	−7.42	6.10	−25.95	21.36	1.507
17.0	0.11	2.12	0.40	7.45	1.927
17.9	0.32	2.17	1.10	7.55	1.528
18.8	1.08	1.10	3.79	3.87	2.599
19.7	1.22	1.30	4.32	4.58	3.208
20.6	1.04	1.17	3.67	4.14	1.659
21.5	1.07	1.37	3.79	4.85	1.413
22.4	0.97	1.13	3.43	3.99	2.123
26.9	1.07	1.08	3.877	3.81	2.675
29.4	1.10	0.86	3.91	3.05	1.019

Fig. 5. Volume integrals per nucleon $[G(E)]$ Eq. (7) around the sensitivity radius calculated for the real (squares) and imaginary (circles) parts of the São Paulo potential. Calculations with slightly different values for R_S (up to 5%) and up to a factor of two for σ were performed with no significant difference in the energy behavior of the integrals.

The depths of the real and imaginary parts of this potential for the ^{9}Be + ^{80}Se system were around 410 MeV, larger than the shallow depths of the Woods–Saxon potential in this work, typically around the tens of MeVs. The resulting fits of the normalization factors and the volume integrals per nucleon for the real and imaginary parts of the São Paulo potential are presented in Table 4 and Fig. 5. It can be seen that their energy dependence, like the ones obtained in Fig. 4 for the Woods–Saxon potential, follow the same shape. The real part decreases in magnitude as the energy falls, even at energies below the Coulomb barrier while the imaginary part increases in the same region. In Fig. 6 a direct comparison between models is performed for the Woods–Saxon EDVG and the São Paulo potentials by means of their respective volume integrals per nucleon.

It is seen in this figure that the shape in energy is the same for both potentials, with a definite decrease of the real part for energies in the vicinity of the Coulomb barrier and an increase of the imaginary part in the same region. This effect could be result of an increment of absorption, as
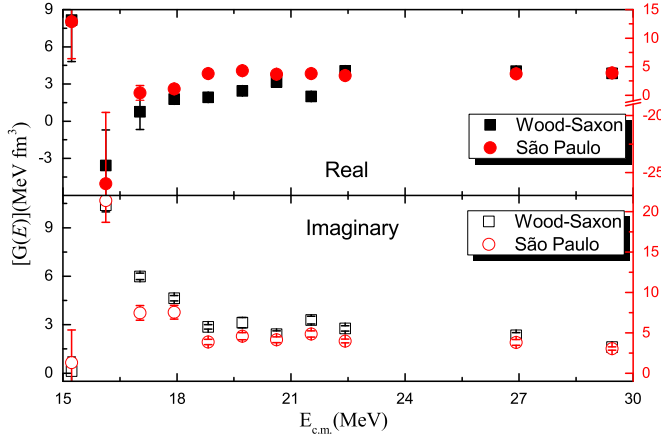
Fig. 6. Volume integrals per nucleon [$G(E)$] Eq. (7) around the sensitivity radius for the real (full symbols) and imaginary (open symbols) parts of the EDVG Woods–Saxon and São Paulo potential.

the energy diminishes, produced by a strong coupling to non-elastic channels that remains open even at sub-coulombian energies. According to Ref. [8,24], this energy behavior is consistent with the breakup threshold anomaly, which is a result of the coupling of the breakup of the weakly bound projectile ^{9}Be to the elastic channel. It also can be seen that the absolute values of the volume integrals for the real part is about the same for both potentials and for the imaginary parts are similar, within the error bars. This fact is of course what one expects, but it is still remarkable to find such an agreement between very different potentials. Of course the "shape" of the volume integrals as a function of the energy is a rather fuzzy concept, often subject to individual interpretation. In order to overcome that problem, we have devised a new method proposed in the following section.

3.2. Dispersion relation through bivariate random sampling

As it was said before, the real and imaginary parts of the volume integrals of the nuclear potential (or equivalently the potentials) are connected through a dispersion relation given by Eq. (7). To calculate this integral, a linear parametrization model was proposed by Satchler [3] which is represented by a series of linear segments. Through these segments, a global shape of the imaginary potential could be modeled. In this work, instead, to fully account for experimental uncertainties we implemented a procedure in which, for each energy, the segment vertices are obtained from random sampling, centered in the adjusted values, following a bivariate normal distribution determined by the covariance matrix [40]

$$f(x_R, x_I) = \frac{1}{\sqrt{(2\pi)^2 \det(V)}} e^{-\frac{1}{2}(\mathbf{x}-\mathbf{x}_0)^T V^{-1}(\mathbf{x}-\mathbf{x}_0)} \tag{9}$$

where $\mathbf{x}_0 = \{x_{R0}, x_{I0}\}$ are the fitted values, V is the covariance matrix defined in Eq. (10) and ρ the correlation factor,

$$V = \begin{bmatrix} \sigma_{x_{R_0}}^2 & \rho \sigma_{x_{R_0}} \sigma_{x_{I_0}} \\ \rho \sigma_{x_{R_0}} \sigma_{x_{I_0}} & \sigma_{x_{I_0}}^2 \end{bmatrix} \tag{10}$$
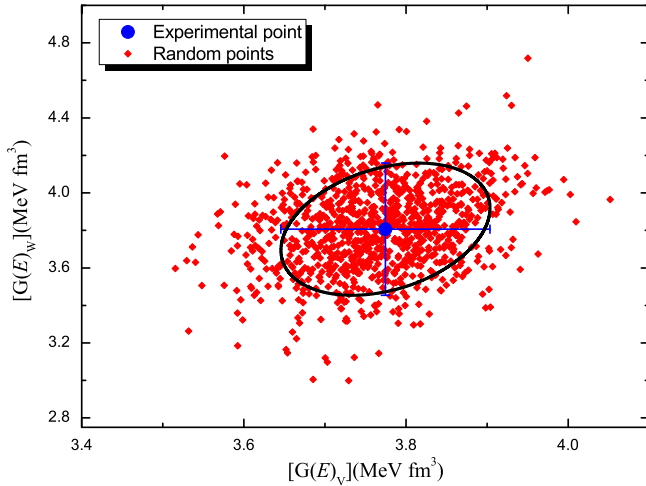
Fig. 7. Random points with a bivariate normal distribution around the experimental volume integrals per nucleon $[G(E)]$ were determined for $E_{c.m.} = 26.9$ MeV. About 68% of the total obtained points lie within the $\chi^2 = \chi_0^2 + 2.3\chi_0^2/\nu$ ellipse.
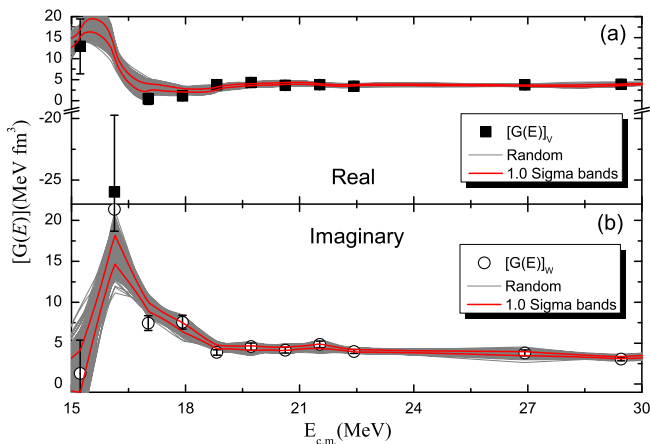

Fig. 8. (a) Imaginary (open circles) and (b) real (solid squares) volume integral per nucleon as a function of the center-of-mass energy for the São Paulo potential. The gray lines in the bottom panel represent the schematic segments lines created from random points following bivariate normal distributions centered at the fitted values (500 lines were drawn). The corresponding upper gray lines are the results of Eq. (7). The red lines represent $\pm 1\sigma$ confidence bands.

In Fig. 7 an example for $E_{c.m.} = 26.9$ MeV is presented for 1000 random points obtained from Eqs. (9) and (10) centered at the volume integrals per nucleon calculated for the São Paulo potential. Each imaginary value from one energy ellipse is then randomly linked to the next one generating a line segment. To avoid nonphysical fluctuations as a function of the energy, the imaginary values at the center were averaged with their closest neighbors with a weight factor. Each of these segments yields a contribution to the real volume integral following the method proposed by Satchler [3]. The graphs are shown in Fig. 8 together with the adjusted values of the volume integrals. It is noteworthy that the best fit for the energy of 16.1 MeV is

obtained for a negative value, both for the real depth V of the Woods–Saxon potential and for the real normalization factor N_R for São Paulo potential. The strong coupling of the breakup channel to the elastic channel could manifest itself in an increment of absorption as the energy diminishes. This implies, by means of the dispersion relation, the appearance of a repulsive polarization real potential that, in cases, could produce a strong diminishing of the total real potential. However, a negative value of the real part of the potential, such as this case, does not necessarily imply a qualitatively different behavior of the scattering wave function. It is rather just an artifact produced by the restriction of geometrical parameters to fixed values (even for the Wood–Saxon EDVG case, in which the variations are quite constrained) for all bombarding energies, over and below the Coulomb barrier.

As it can be seen in Fig. 8, the adjusted real volume integrals per nucleon, except for the point at 16.1 MeV, lie within the $\pm 1\sigma$ confidence bands of the random points at each energy in the range from 15 to 33 MeV. Based on this criterion, it is concluded that the overall behavior of the real and imaginary integrals per nucleon (or equivalently, the potentials) follows the dispersion relation of Eq. (7) consistently with the calculated parameter uncertainties. The decrease of the real potential at energies below 17.9 MeV and the consequent increase of the imaginary potential, unambiguously indicate a behavior consistent with the breakup threshold anomaly.

4. Summary and conclusions

Elastic scattering angular distributions for the ^{9}Be + ^{80}Se system were measured at eleven energies around the Coulomb barrier. The experimental data were analyzed on the framework of the optical model using two different potentials: a phenomenological Woods–Saxon potential and the double folding São Paulo potential. For these two potentials, the imaginary potential peaked at a bombarding energy close to the Coulomb barrier, whereas the real part presented a minimum. Through a robust treatment of experimental uncertainties, we show that this behavior is clearly consistent with the breakup threshold anomaly proposed for weakly bound projectiles. This effect is the result of the strong coupling of the breakup channel to the elastic one that produces a dynamic polarization potential that remains important even at energies below the Coulomb barrier. The dispersion relation for the real and imaginary parts of the optical potential was calculated with a new method based on bivariate random sampling. This method allows us to conclude that the energy behavior of the real and imaginary potentials is also compatible with the dispersion relation.

Acknowledgements

References

[1] L.F. Canto, P.R.S. Gomes, R. Donangelo, M.S. Hussein, Phys. Rep. 424 (2006) 1.
[2] M.A. Nagarajan, C.C. Mahaux, G.R. Satchler, Phys. Rev. Lett. 54 (1985) 1136.
[3] G.R. Satchler, Phys. Rep. 199 (1991) 147.
[4] J.O. Fernández Niello, J.M. Figueira, D. Abriola, A. Arazi, O.A. Capurro, G.V. Martí, D. Martínez Heinmann, A.J. Pacheco, E. de Barbará, I. Padrón, P.R.S. Gomes, J. Lubian, Nucl. Phys. A 787 (2007) 484.
[5] M. Biswas, S. Roy, M. Sinha, M.K. Pradhan, A. Mukherjee, P. Basu, H. Majumdar, K. Ramachandran, A. Shrivastava, Nucl. Phys. A 802 (2008) 67.

[6] N.N. Deshmukh, S. Mukherjee, D. Patel, N.L. Singh, P.K. Rath, B.K. Nayak, D.C. Biswas, S. Santra, E.T. Mirgule, L.S. Danu, Y.K. Gupta, A. Saxena, R.K. Choudhury, R. Kumar, J. Lubian, C.C. Lopes, E.N. Cardozo, P.R.S. Gomes, Phys. Rev. C 83 (2011) 024607.

[7] A.M.M. Maciel, P.R.S. Gomes, J. Lubian, R.M. Anjos, R. Cabezas, G.M. Santos, C. Muri, S.B. Moraes, R.L. Neto, N. Added, N.C. Filho, C. Tenreiro, Phys. Rev. C 59 (1999) 2103.

[8] M.S. Hussein, P.R.S. Gomes, J. Lubian, L.C. Chamon, Phys. Rev. C 73 (2006) 044610.

[9] A. Gómez Camacho, E. Aguilera, E. Martínez Quiroz, P. Gomes, J. Lubian, L. Canto, Nucl. Phys. A 883 (2010) 158.

[10] L. Fimiani, J.M. Figueira, G.V. Martí, J.E. Testoni, A.J. Pacheco, W.H.Z. Cárdenas, A. Arazi, O.A. Capurro, M.A. Cardona, P. Carnelli, E. de Barbará, D. Hojman, D. Martínez Heimann, A.E. Negri, Phys. Rev. C 86 (2012) 044607.

[11] J.M. Figueira, J.O. Fernández Niello, A. Arazi, O.A. Capurro, P. Carnelli, L. Fimiani, G.V. Martí, D. Martínez Heimann, A.E. Negri, A.J. Pacheco, J. Lubian, D.S. Monteiro, P.R.S. Gomes, Phys. Rev. C 81 (2010) 024613.

[12] F.A. Souza, L.A.S. Leal, N. Carlin, M.G. Munhoz, R. Liguori Neto, M.M. de Moura, A.A.P. Suaide, E.M. Szanto, A. Szanto de Toledo, J. Takahashi, Phys. Rev. C 75 (2007) 044601.

[13] N. Keeley, S.J. Bennett, N.M. Clarke, B.R. Fulton, G. Tungate, P.V. Drumm, M.A. Nagarajan, J.S. Lilley, Nucl. Phys. A 571 (1994) 326.

[14] A. Pakou, N. Alamanos, G. Doukelis, A. Gillibert, G. Kalyva, M. Kokkoris, S. Kossionides, A. Lagoyannis, A. Musumarra, C. Papachristodoulou, N. Patronis, G. Perdikakis, D. Pierroutsakou, E.C. Pollacco, K. Rusek, Phys. Rev. C 69 (2004) 054602.

[15] A. Gomez Camacho, P.R.S. Gomes, J. Lubian, E.F. Aguilera, I. Padrón, Phys. Rev. C 76 (2007) 044609.

[16] P.R.S. Gomes, R.M. Anjos, C. Muri, J. Lubian, I. Padron, L.C. Chamon, R. Liguori Neto, N. Added, J.O. Fernández Niello, G.V. Martí, O.A. Capurro, A.J. Pacheco, J.E. Testoni, D. Abriola, Phys. Rev. C 70 (2004) 054605.

[17] P.R.S. Gomes, J. Lubian, B. Paes, V.N. Garcia, D. Monteiro, I. Padrón, J.M. Figueira, A. Arazi, O.A. Capurro, L. Fimiani, A.E. Negri, G.V. Martí, J.O. Fernández Niello, A. Gómez-Camacho, L.F. Canto, Nucl. Phys. A 828 (2009) 233.

[18] J. Lubian, I. Padrón, P.R.S. Gomes, A.M.M. Maciel, R.M. Anjos, S.B. Moraes, J.J.S. Alves, C. Muri, R. Liguori Neto, N. Added, Phys. Rev. C 64 (2001) 027601.

[19] J.M. Figueira, D. Abriola, J.O. Fernández Niello, A. Arazi, O.A. Capurro, E. de Barbará, G.V. Martí, D. Martínez Heimann, A.J. Pacheco, J.E. Testoni, I. Padrón, P.R.S. Gomes, J. Lubian, Phys. Rev. C 73 (2006) 054603.

[20] R. Oliveira, N. Carlin, R. Liguori Neto, M. de Moura, M. Munhoz, M. del Santo, F. Souza, E. Szanto, A. Szanto de Toledo, A. Suaide, Nucl. Phys. A 856 (2011) 46.

[21] Y. Sakuragi, Phys. Rev. C 35 (1987) 2161.

[22] A. Pakou, N. Alamanos, A. Lagoyannis, A. Gillibert, E.C. Pollacco, P.A. Assimakopoulos, G. Doukelis, K.G. Ioannides, D. Karadimos, D. Karamanis, M. Kokkoris, E. Kossionides, N. Nicolis, C. Papachristodoulou, N. Patronis, G.P.D. Pierroutsakou, Phys. Lett. B 556 (2003) 21.

[23] C. Signorini, A. Andrighetto, M. Ruan, J.Y. Guo, L. Stroe, F. Soramel, K.E.G. Löbner, L. Müller, D. Pierroutsakou, M. Romoli, K. Rudolph, I.J. Thompson, M. Trotta, A. Vitturi, R. Gernhäuser, A. Kastenmüller, Phys. Rev. C 61 (2000).

[24] M.S. Hussein, P.R.S. Gomes, J. Lubian, L.C. Chamon, Phys. Rev. C 76 (2007), 019902(E).

[25] A. Arazi, J. Casal, M. Rodríguez-Gallardo, J.M. Arias, R. Lichtenthäler Filho, D. Abriola, O.A. Capurro, M.A. Cardona, P.F.F. Carnelli, E. de Barbará, J. Fernández Niello, J.M. Figueira, L. Fimiani, D. Hojman, G.V. Martí, D. Martínez Heimman, A.J. Pacheco, Phys. Rev. C 97 (2018) 044609.

[26] A. Gómez Camacho, P.R.S. Gomes, J. Lubian, Phys. Rev. C 82 (2010) 067601.

[27] P.R.S. Gomes, M.D. Rodriguez, G.V. Martí, I. Padrón, L.C. Chamon, J.O. Fernández Niello, O.A. Capurro, A.J. Pacheco, J.E. Testoni, A. Arazi, M. Ramírez, R.M. Anjos, J. Lubian, R. Veiga, R. Liguori Neto, E. Crema, N. Added, C. Tenreiro, M.S. Hussein, Phys. Rev. C 71 (2005) 034608.

[28] D. Abriola, A. Arazi, J. Testoni, F. Gollan, G.V. Martí, J. Phys. 630 (2015) 012021.

[29] J. Wilczynski, K. Siwek-Wilczynska, Phys. Lett. B 55 (1975) 270.

[30] D. Abriola, A.A. Sonzogni, M. di Tada, A. Etchegoyen, M.C. Etchegoyen, J.O. Fernández Niello, S. Gil, A.O. Macchiavelli, A.J. Pacheco, R. Piegaia, J.E. Testoni, Phys. Rev. C 46 (1992) 244.

[31] M.H. Macfarlane, S.C. Pieper, Argonne National Laboratory Report ANL-76-11 (1978), unpublished.

[32] W.H. Press, et al., Numerical Recipes, third edition, Cambridge University Press, Cambridge CB2 8RU, UK, 2007.

[33] M.E. Brandan, J.R. Alfaro, A. Menchaca-Rocha, J. Gómez del Campo, G.R. Satchler, P.H. Stelson, H.J. Kim, D. Shapira, Phys. Rev. C 48 (1993) 1147.

[34] C. Mahaux, H. Ngô, G.R. Satchler, Nucl. Phys. A 449 (1986) 354.

[35] C. Mahaux, H. Ngô, G.R. Satchler, Nucl. Phys. A 456 (1986) 134.
[36] L.C. Chamon, D. Pereira, M.S. Hussein, M.A. Cândido Ribeiro, Phys. Rev. Lett. 79 (1997) 5218.
[37] L.C. Chamon, B.V. Carlson, L.R. Gasques, D. Pereira, C. De Conti, M.A.G. Alvarez, M.S. Hussein, M.A. Cândido Ribeiro, E.S. Rossi Jr., C.P. Silva, Phys. Rev. C 66 (2002) 014610.
[38] M.A.G. Alvarez, L.C. Chamon, M. Hussein, D. Pereira, L.R. Gasques, E.S. Rossi, C.P. Silva, Nucl. Phys. A 723 (2003) 93.
[39] M.A. Cândido Ribeiro, L.C. Chamon, D. Pereira, M.S. Hussein, D. Galetti, Phys. Rev. Lett. 78 (1997) 3270.
[40] D. Abriola, G.V. Marti, J.E. Testoni, EPJ Web Conf. 146 (2017) 02050.